Comparison of Higher-Order CFD Modelling with an Unsteady Panel Method

Gunther Wilke

German Aerospace Center (DLR) - Institute of Aerodynamics and Flow Technology, Braunschweig, Germany

One major difficulty in the design of quiet rotor blades is the correct numerical prediction of blade vortex interaction (BVI) noise in descent flight. Current second order spatial discretization schemes inherently have too much numerical dissipation to correctly conserve vorticity in the computational fluid dynamics (CFD) simulation. Higher order methods have proven their worthiness to alleviate this problem, yet are costly in terms of computational resources. In this paper, the 4^{th} order implicit compact Pade scheme based on the finite difference formulation of the RANS equations is employed to convect the vortices in the simulation. The approach is paired with the classical finite volume approach with the Jameson-Schmidt-Turkel (JST) scheme. The robustness and flexibility of the JST scheme are exploited in the near field of the rotor blades and fuselage, while in the mid- and farfield the Pade scheme is utilized. This approach is validated against the experimental data of the HART II wind tunnel campaign. Opposing this higher order approach, a classical panel method with a free wake model is investigated. It allows for the computation of results at similar quality of the higher order CFD scheme, however at a much reduced price. In this paper the effect of grid densities for all methods is analyzed along with the direct comparison of them for the resolution of BVI noise in descent flight of the HART II test case.

I. INTRODUCTION

Helicopters are noisy in their operation. Especially in the descent flight condition upon the landing approach, a slapping of the rotor is heard. This phenomenon is known as blade-vortex interaction (BVI) noise. The tip vortices that trail off the blades are hit again by the following blades. In particular when these vortices are parallel to the passing blade, a fast change of angle-of-attack occurs on the blade leading to sudden changes in the airloads on the blade. This effect causes most of the noise generated in the descent flight condition, which is also considered during certification. The helicopter must stay under specified noise limits during the approach. Therefore it is highly beneficial for aircraft manufactures to properly predict the rotor noise before it is built.

There is much ongoing research concerning the simulation of BVI noise. The popular test campaign HART-II[1] investigates a scaled BO-105 rotor model in detail in various flight conditions including the BVI dominant descent flight. The purpose of this campaign is to analyze the effect of higher-harmonic controls (HHC) of the rotor blades onto BVI noise. The HART-II test campaign is well documented and therefore creates a good basis for simulation code validation. Smith et al.[2] compare various computational fluid-structural dynamics codes against the experimental HART-II data. Their observation is that the spatial and temporal accuracy of the simulation is crucial for the successful simulation of BVI noise. They state that second order spatial accuracy is insufficient on typical engineering meshes and this is either alleviated by increasing the grid density in regions of interest through mesh adaptation or spatial schemes of higher order accuracy. Recent works by Lim et al.[3] demonstrate that grid refinement greatly contributes to the correct vorticity prediction. Jain et al.[4] proof that a 5^{th} order spatial scheme also enhances the vorticity prediction. Tanabe and Sugawara[5] implement a higher order upwind scheme and demonstrate that it is well suited for vortex conservation. All these works have one thing in common; they split the computational domain into zones with different solution strategies. They compute the near-body grids with a second order finite volume method and apply a higher order scheme in the farfield, which may even be temporally decoupled.

A different approach is gone by Kowarsch et al.[6] for the simulation of BVI noise. They apply the 5^{th} order WENO scheme in the whole computational domain, which is robust but also costly since the WENO scheme evaluates multiple stencils for one cell to combine them in the most optimal way.

In contrast to the high-fidelity CFD tools, there exist tools that are not based on first principles that still predict BVI noise with reasonable accuracy. van der Wall et al.[7] present a wholesome investigation of the HARTII test case with comprehensive codes. The merits of these codes are the fast turn-around times in comparison with CFD and in case of BVI noise may even achieve better results. An intermediate stage of physical modelling depth is given by panel based approaches. Yin et al.[8] investigate the feasibility of such a panel method for the prediction of helicopter noise in different flight conditions. While the results of this unsteady panel method deviate from the wind tunnel results for the flight conditions of climb and fast forward flight, they reliable reproduce the BVI noise event.

Motivation of this work is to compare a new efficient higher-order scheme for the simulation of the HART-II test case with the aforementioned panel method. The CFD scheme is a compact implicit higher-order finite difference scheme, the Pade scheme developed by Lele.[9] Due to its implicit nature it is solved quickly in contrast to other schemes. It is also utilized in a zonal approach, where the rotor blades are still modeled with the second order finite-volume scheme by James-Schmidt-Turkel (JST)[10] referred to as a Hybrid simulation or scheme in this paper. Despite the efficient nature of this higher order scheme, the computational effort is tremendous relative to the panel method. The quality of the results is compared against each other and recommendations for future applications and research is given.

II. METHODOLOGY

For the complete and correct simulation of the helicopter, the blade aero-mechanics need to be solved including the disciplines of aero-, structural- and flight dynamics. Therefore, the simulation of the HART II test case consists of the application of the comprehensive code HOST[11] developed by Airbus Helicopters France to account for the structural- and flight dynamics and the block-structured flow solver FLOWer[12] or the unsteady panel method (UPM),[13] both developed by DLR. The code coupling is validated for FLOWer and HOST by Dietz et al.[14] and by Yin et al.[8] for UPM and HOST.

A. Acoustic Computation

The evaluation of the noise carpets is done through using the Ffowcs WilliamsHawkings (FW-H) equations. The input data for the FW-H equations are utilized in the (elastic) Farasat 1A formulation,[15] which allows to simply use the deformed blade pressure surface as input data. The blade pressure is then computed either by CFD with FLOWer or with UPM. The FW-H code is APSIM developed by DLR.[16]

B. CFD Strategy

The block-structured solver FLOWer allows the computation of different numerical schemes on different blocks in the computational domains. This is exploited for the sake of stability in the simulation and sketched in Fig. 1. The individual regions are marked with different colors. The rotor blades are computed with the 2^{nd} order JST scheme, while the fuselage is computed with a mixed version of JST and Pade scheme, where the flux calculation is based on JST and the numerical dampening is based on a 6^{th} order Pade filter. The background mesh is purely computed with the 4^{th} order Pade Scheme also applying the 6th order Pade filter.

For the following investigation, two types of simulations are setup:

- Inviscid Euler simulation of an isolated rotor (inviscid CFD)
- Viscous Reynolds-Average Navier-Stokes (RANS) simulation of the rotor with the fuselage (viscous CFD)

The viscous simulations employ the Wilcox $k-\omega$ turbulence model[17] for the calculation of the turbulent viscosity. The reason for these three setups is to determine how much detail is required in the simulation to capture the noise signature of the BVI dominant descent flight.

The time is advanced with a 2^{nd} order dual-time stepping scheme, where the inner iterations are computed with a five-stage Runge-Kutta scheme. For the blade and fuselage grids, three levels of multigrid accelerate

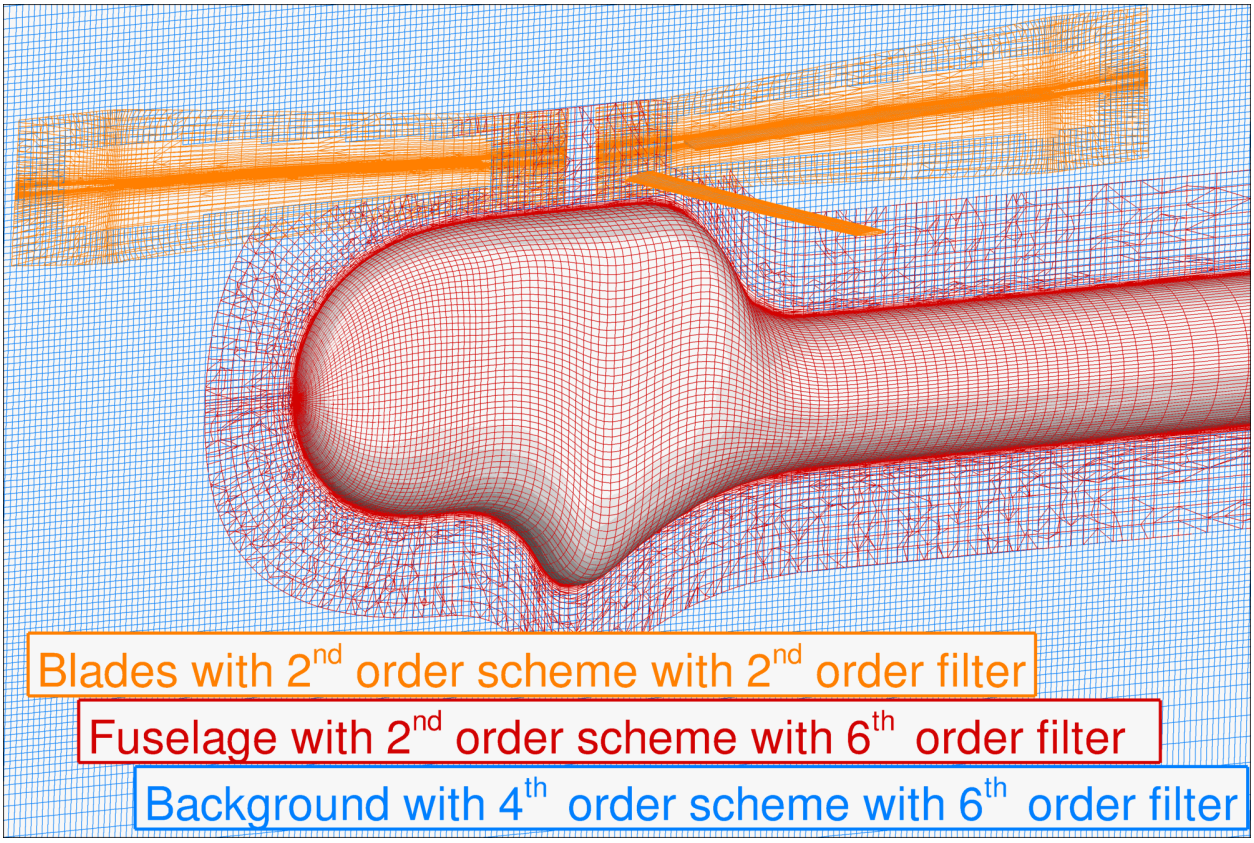

Figure 1. Schematic of the employment of different numerical schemes.

the convergence, while additionally the Runge-Kutta scheme is implicitly smoothed. The corresponding Courant-Friedrichs-Lewy (CFL) number is chosen to be 7.5.

1. *Discretization*

The frequency range of BVI noise is roughly between 6-40 blade passing frequencies (BPF). This means that a frequency of roughly $1400Hz$ has to be resolved for the upper limit. Using the speed of sound, this yields a minimum wave length of $0.246m$. Assuming the occurring signals are resolved with 10 discretization points, a time step of $3.6 \cdot 10^{-5}s$ is required and a grid spacing of $0.0123m$. This corresponds to a time step equivalent of $\Delta\psi = 0.23^o$ and 10% chord lengths in spacing.

level	coarse	medium	fine
blade	40,392	323,136	2,585,088
fuselage	61,440	491,520	3,932,160
background	1,382,400	11,059,200	88,473,600
total	1,605,408	12,843,264	102,746,112

Table 1. FLOWer grid sizes at different (multigrid-)levels

While the time step has an effect on the overall simulation, the grid spacing is most critical for the design of the background mesh. The background mesh is created using an equidistant spacing near the rotor disc and the rotor wake and grows exponentially towards the farfield. Thus, about half the points of the background mesh are in the inner domain, the other half grows towards the farfield. A sketch of the inner and outer part of the background mesh along with its dimensions is shown in Fig. 2.

The blade grid generation is done with an in-house grid generator based on the principles of transfinite

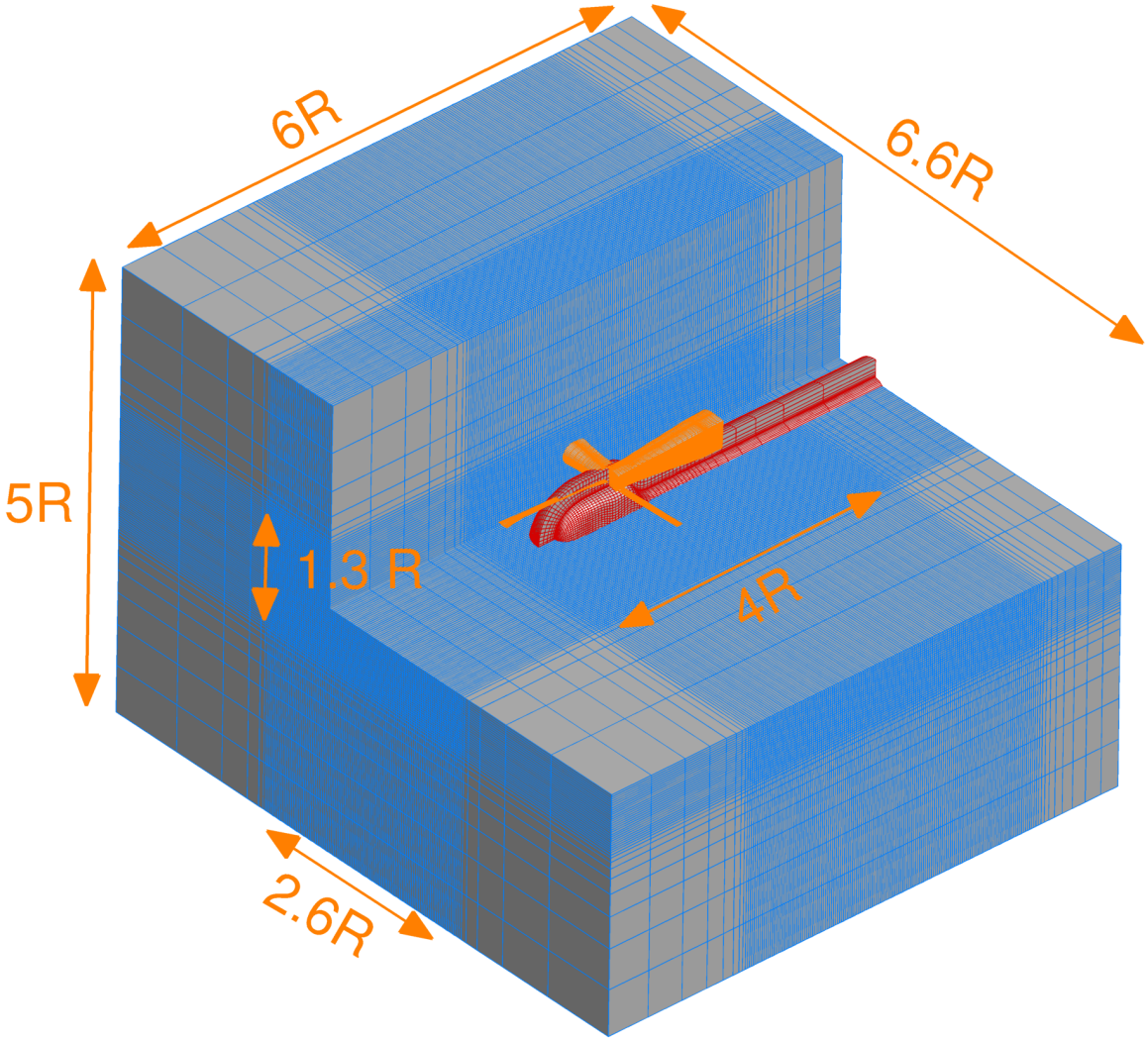

Figure 2. Schematic of background mesh and its dimensions

interpolation[18] and enhanced for boundary layer treatment as well as multi-block structures. The inviscid mesh topology is of the type O-H, while the viscous meshes are of the C-H type. For the inviscid meshes, the root, tip and tab of the blade are modified. Instead of utilizing the airfoil of the HART II test campaign, which is a modified NACA23012, the original version of the NACA23012 being closed at the trailing edge is utilized. The blade tip and root are tapered and therefore not blunt as the wind tunnel model. The RANS meshes resemble the wind tunnel geometry closely. The criterion of $y^+ = 1$ for the finest grid spacing in the wall normal direction is fulfilled throughout the surface, with the exception that the blade root and tip go beyond $y^+ = 1$ to not overly increase the number of required grid points. Both blade tip treatments, inviscid and viscous are visually compared in Fig. 3 and their individual topologies in Fig. 4.

Three levels of refinement are investigated, see Table 1, which are coarse, medium and fine. The coarse and medium levels are generated from the finest level by leaving out every other grid point in each spatial direction. The distribution of points is listed in Table 2 for the finest level. Accompanying the spatial resolution, the temporal resolution is additionally increased, which is listed in Table 3.

Since the wake of the rotor requires time to be evolved, the formula $N_{revolutions} = 1/\mu\pi$ has been established to estimate this required time. The formula reflects the time in number of rotor revolutions a particle needs when it is released at the front of the rotor disc to leave at the aft of the disc in dependency of the advance ratio μ. For the HART II case, which has an advance ratio of 0.15 see Table 6, this leads to

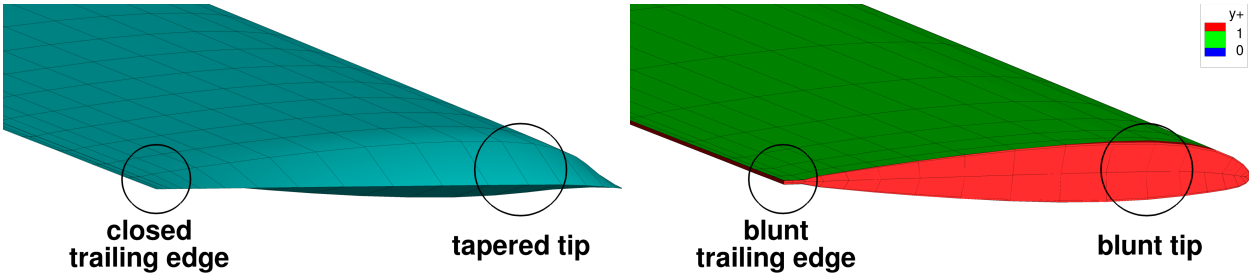

(a) Euler Mesh (b) RANS Mesh

Figure 3. The blade tips and tabs shown for the different discretizations (coarsest grid level)

mesh	**inviscid**			**viscous**		
blade	chordwise	radial	normal	chordwise	radial	normal
	161	24+73+48	65	145 + 2 x 41	24+73+48	73
	= 2,211,840 cells			**= 2,585,088 cells**		
fuselage				lengthwise	radial	normal
				257	241	65
				= 3,932,160 cells		
background	inflight		lateral		vertical	
(inner)	554		422		210	
(total)	641		481		289	
	=88,473,600 cells					
total	**= 97,320,960 cells**			**= 98,813,952 cells** without fuselage **= 102,746,112 cells** with fuselage		

Table 2. FLOWer discretization of the blade for the individual solution strategies at the finest level

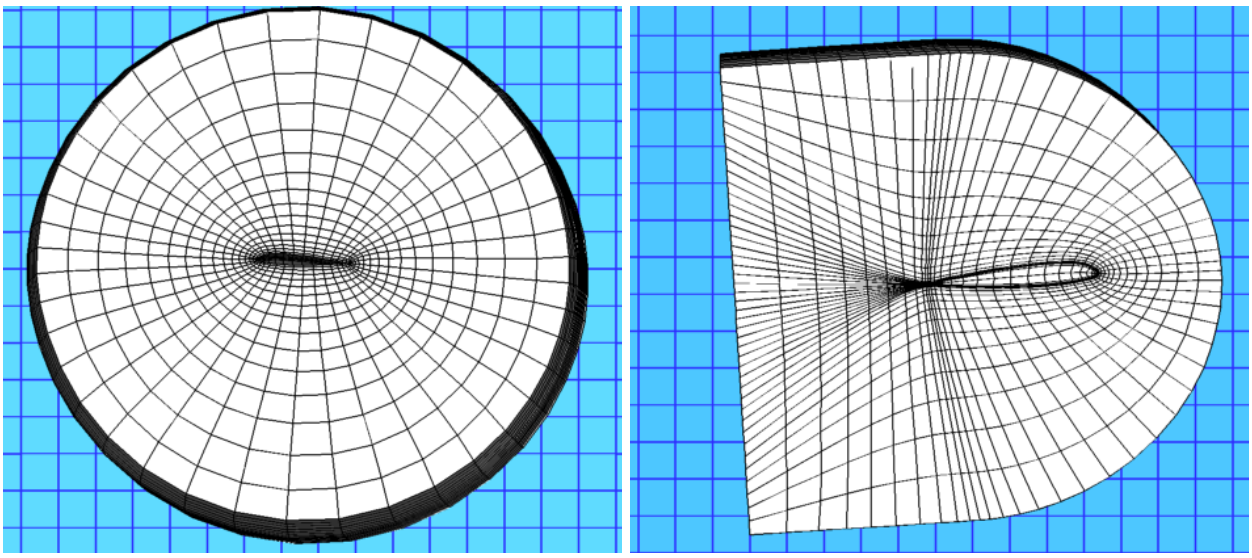

(a) Euler Mesh (b) RANS Mesh

Figure 4. Blade topologies shown with the inner background mesh spacing for the coarse mesh setups

level	equivalent time step	initial revolutions	consequetive revolutions per trim iteration
coarse	2.00^o		
medium	0.50^o	4	2
fine	0.25^o		

Table 3. FLOWer temporal settings assoziated with the different resolutions.

roughly two revolutions. For the initial coupling iteration, another two revolutions are utilized to ensure a periodic signal and then each consequetive coupling step is performed with two revolutions.

2. Jameson-Schmidt-Turkel Scheme

For the blade grids, the James-Schmidt-Turkel (JST)[10] scheme is utilized for the spatial representation of the fluxes of the Navier-Stokes equations. The scheme is based on the volume formulation and shows a very robust behavior. The discrete form of JST is stated as:

$$\frac{d}{dt}\vec{W}_{i,j,j} \cdot V_{i,j,k} + \vec{Q}_{i,j,k} + \vec{G}_{i,j,k} \cdot V_{i,j,k} - \vec{D}_{i,j,k} = 0 \tag{1}$$

with $\vec{W}$ the conservative variables, V the volume, $\vec{Q}$ the surface integral over the fluxes, $\vec{G}$ the source terms for the rotating frame and $\vec{D}$ a numerical dissipation operator at the index location i, j, k. The flux integral $\vec{Q}$ is approximated by the six face of the hexaedric control volume:

$$\vec{Q}_{i,j,k} = \sum_{s}^{6} (\bar{\bar{F}}_t - \vec{W}_t \cdot \vec{q}_{b_t}) \cdot \vec{S}_s \tag{2}$$

with $\bar{\bar{F}}$ the flux density tensor, $\vec{q}_{b_t}$ the motion of the grid cell and $\vec{S}_s$ the surface normal vector. The index t is to be replaced by $i \pm \frac{1}{2}, j, k$ for $t = 1, 2$, $i, j \pm \frac{1}{2}, k$ for $t = 3, 4$, and $i, j, k \pm \frac{1}{2}$ for $t = 5, 6$. The half index $\pm\frac{1}{2}$ denotes the flux averaging which is done to evaluate the value of two cells at the intersecting cell face. The flux density is therefore computed by

$$\bar{\bar{F}}_{i-\frac{1}{2},j,k} = \bar{\bar{F}}(\vec{W}_{i-\frac{1}{2},j,k}) \tag{3}$$

with

$$\vec{W}_{i-\frac{1}{2},j,k} = \frac{1}{2}(\vec{W}_{i-1,j,k} + \vec{W}_{i,j,k}). \tag{4}$$

This alone yields a formally second order accurate scheme. However, it is not stable over discontinuities by itself and therefore JST implemented the numerical dissipation operator $\vec{D}$, which is similarly evaluated as the surface integral:

$$\vec{D}_{i,j,k} = \sum_{t}^{3} (\vec{d}_{t+\frac{1}{2}} - d_{t-\frac{1}{2}}) \tag{5}$$

with t again the interchanging offset of i, j, k. The dissipative flux $d_{i+\frac{1}{2},j,k}$ is calculated by:

$$\begin{aligned} d_{i+\frac{1}{2},j,k} &= \epsilon^{(2)}_{i+\frac{1}{2},j,k}(\vec{W}_{i+\frac{1}{2},j,k} - \vec{W}_{i,j,k}) \\ -\epsilon^{(4)}_{i+\frac{1}{2},j,k}&(\vec{W}_{i+2,j,k} - 3\vec{W}_{i+1,j,k} + 3\vec{W}_{i,j,k} - \vec{W}_{i-1,j,k}) \end{aligned} \tag{6}$$

The coefficients $\epsilon^{(2)}_{i+\frac{1}{2},j,k}$ for strong gradients and $\epsilon^{(4)}_{i+\frac{1}{2},j,k}$ for high-frequency oscillations are computed by:

$$\epsilon^{(2)}_{i+\frac{1}{2},j,k} = k^{(2)} max(\nu_{i,j,k}, \nu_{i+1,j,k}) \tag{7}$$

$$\epsilon^{(4)}_{i+\frac{1}{2},j,k} = max(0, k^{(4)} - \epsilon^{(2)}_{i+\frac{1}{2},j,k}) \tag{8}$$

with the pressure sensor

$$\nu_{i,j,k} = \left| \frac{p_{i-1,j,k} - 2p_{i,j,k} + p_{i+1,j,k}}{p_{i-1,j,k} + 2p_{i,j,k} + p_{i+1,j,k}} \right|. \tag{9}$$

and $p_{i,j,k}$ the pressure in cell i, j, k. The coefficents $k^{(2)}$ and $k^{(4)}$ are chosen to be $\frac{1}{2}$ and $\frac{1}{128}$ in this work.

3. Compact Pade Scheme

The concept of the Pade scheme is to solve the Navier-Stokes equations on a equidistant, Cartesian mesh. As this is not necessarily the case (the background mesh only partially fulfills this condition), a coordinate transformation from a curvilinear grid to the Cartesian grid is necessary. The Navier-Stokes equations in the transformed finite-difference formulation read:

$$\frac{d}{dt}\frac{\vec{W}}{J} + \sum_{i=1}^{3} \frac{\partial \hat{F}_i}{\partial \xi_i} + \frac{\hat{\vec{G}}}{J} = 0 \tag{10}$$

The flux density tensor is now altered $\hat{F}$ and built with the contravariant velocity $\hat{U}$:

$$\hat{F}_i = \begin{bmatrix} \rho\hat{U}_i \\ \rho u\hat{U}_i + \xi_{i_x} p \\ \rho v\hat{U}_i + \xi_{i_y} p \\ \rho w\hat{U}_i + \xi_{i_z} p \\ (\rho E + p)\hat{U} - \xi_{i_t} p \end{bmatrix} \tag{11}$$

Additionally the determinant of Jakobian J of the Cartesian coordinates $\vec{\xi} = (\xi, \eta, \zeta)^T$ of the equidistant mesh is introduced:

$$J = \begin{vmatrix} x_\xi & y_\xi & z_\xi \\ x_\eta & y_\eta & z_\eta \\ x_\zeta & y_\zeta & z_\zeta \end{vmatrix} \tag{12}$$

For a more detailed discussion on the coordinate transformation, in particular for moving meshes, see Visbal and Gaitonde.[19] With the Navier-Stokes equations in the finite-difference form, the ansatz of the Pade scheme can be utilized. The general equation for the approximation of a first difference of a function ϕ of 2^{nd} to 6^{th} order according to Lele[9] is:

$$\sum_{i=-1}^{1} \alpha_i \phi_i^{(1)} = \sum_{i=1}^{3} \frac{c_i}{2ih} (\phi_{+i} - \phi - i) \tag{13}$$

with i being an index, α_i the coefficients for the derivatives, c_i the coefficients for the original cell values, and h the cell spacing. Thus, the Pade scheme poses a line-implicit tri-diagonal system of equations, which can be efficiently solved by the Thomas algorithm. To numerically stabilize the scheme, the Pade filter is postulated as:

$$\alpha_f \tilde{\phi}_{i+1} + \tilde{\phi}_i + \alpha_f \tilde{\phi}_{i-1} = \sum_{n=0}^{N} \frac{a_n}{2} (\phi_{i+1} - \phi_{i-1}) \tag{14}$$

with $\tilde{\phi}$ being the filtered function value, n the index distance from the current cell i and N being the total width of the filter. α_f is the filter constant, which analogous to $k^{(2)}$ and $k^{(4)}$ for the JST scheme allows to control the amount of filtering. It may be chosen between $-\frac{1}{2}$ and $\frac{1}{2}$. $\alpha_f = -\frac{1}{2}$ is the most dissipative setting and $\frac{1}{2}$ the least. In this work, α_f is chosen to be 0.499 and $N = 3$, which corresponds to a 6^{th} order filtering. The system of equations for the linear filter is also tri-diagonal and is solved the same way as the Pade scheme. To keep the accuracy within in the physical domain at 4^{th} order, four dummy layers are added to each block boundary for the data exchange between blocks, while it is only two dummy layers for the JST scheme.

The scheme is implemented as a cell-centered version into FLOWer by Enk.[20] The adaptation of the Chimera scheme is done according to Sherer and Scott,[21] who end the implicit line at the beginning of a hole and restart the line after the hole as a new line through the adjustment of the coefficients.

scheme	JST	Pade
formulation	integral, finite-volume	transformed finite difference
solution type	explicit	line-implicit, tri-diagonal
metric	cell centered	
max formal order	2^{nd}	4^{th}
min formal order	1^{st}	4^{th}
filtering	2^{nd} and 4^{th}	6^{th}, (4^{th}, 8^{th})
shock-capturing	yes, through pressure sensor	no
low-pass filtering	4^{th} order	6^{th} order
recommended application	near wall meshes (due to grid quality), high gradient flows (shocks)	(farfield) vorticity transport, subsonic turbulent flows, (DNS/LES)

Table 4. Comparison of the major attributes of the JST and Pade scheme as implemented in the FLOWer code

4. Scheme Comparison

The major differences of the JST and Pade scheme are highlighted in the Table 4. Essentially, the JST scheme is a very robust scheme, which is able to compute a lot of different flow cases. However, the robustness comes at the price of increased numerical damping. Especially the modelling of the tip vortices becomes difficult with this scheme, as a high spatial (and temporal) resolution is necessary. The Pade scheme, through its higher order and low dissipative filtering proves to be very valuable for this task. However, with the necessary grid transformation and the inability to directly treat discontinuities such as shock waves, it is less suited for the blade grids. The grid quality requirements are a lot stricter for the Pade scheme than for the JST scheme. A negative determinant is more easily generated than a negative volume!

C. UPM Strategy

The unsteady panel method developed by DLR is specifically tailored to rotor applications. It assumes inviscid, irrotational, incompressible potential flow to model the rotor blade and the according wake. Since viscosity is important for obtaining a correct trim condition,[22] UPM is only coupled one way. This means that the trim condition is purely obtained by the comprehensive code HOST and UPM is then used for the computation of the BVI noise. In order to improve the trim solution obtained by HOST, the prescribed wake model METAR[23] is employed to enhance the results of the computed inflow.

1. Discretization

In contrast to CFD, UPM is a surface singularity method. Since the flow is modeled by potential functions, the need for a high spatial as well as temporal resolution is alleviated in contrast to CFD. The assumption is that the potential functions sufficiently accurately mimic the behavior of the flow and the resolution thus is almost exclusively required to record the occurring physical effects.

In UPM, the resolution for the blade and fuselage surface, the time step, and the wake have to be chosen. For the blade this is the chord- and spanwise number of panels, while for the wake the radial resolution as well as its length to be kept are important. Similar to the FLOWer computations, multiple resolutions are tried. Their specific values are listed in Table 5. In contrast to CFD, the blade root and tip are not closed, since two potentials too close to each other might lead to numerical instabilities. Also the tab of the airfoil is closed abruptly for this purpose to taper into the trailing wake panels, see Fig. 5(a)

2. Theory

The general solution process of UPM is as follows: First the pressure distribution und lift is determined on the blade, and then the rotor wake is evolved.

For the first part, the rotor blade surface is represented by a source/sink distribution, see Fig. 5(b). Within the airfoil, a vortex sheet is placed, which is represented by a single vortex, however its distribution is scaled along this sheet with the airfoil thickness. The airfoil is closed at the trailing edge with the Kutta

level	coarse	medium	fine
timestep	2.0^o	1.5^o	1.0^o
blade	48x10	72x15	96x20
	=480	=1,080	=1,920
fuselage		32x30	
		=960	
wake	x 1.5 rev	x 2 rev	x 3 rev
	10,800	28,800	86,400
total	13,680	34,080	95,040

Table 5. UPM temporal and spatial resolution of the HART II case. NOTE: number of wake panels grows with timestep, the length of the wake as well as the number of radial locations

Panel, on which the Kutta-Joukouwski theorem is enforced. In a steady computation, this is achieved by solving the linear system of equations and setting the velocity on the Kutta-Panel to be parallel to it. However, in an unsteady Panel method, it has been shown that this is insufficient. Thus the unsteady pressure Kutta condition[24] is ensured through an iterative Newton approach. The pressure on the upper and lower surface is sought to be equal by varying the vortex strength of the blade section, considering the unsteady Bernoulli equation. As a starting solution, the steady solution of the Kutta condition is utilized, where tangential flow has been assumed.

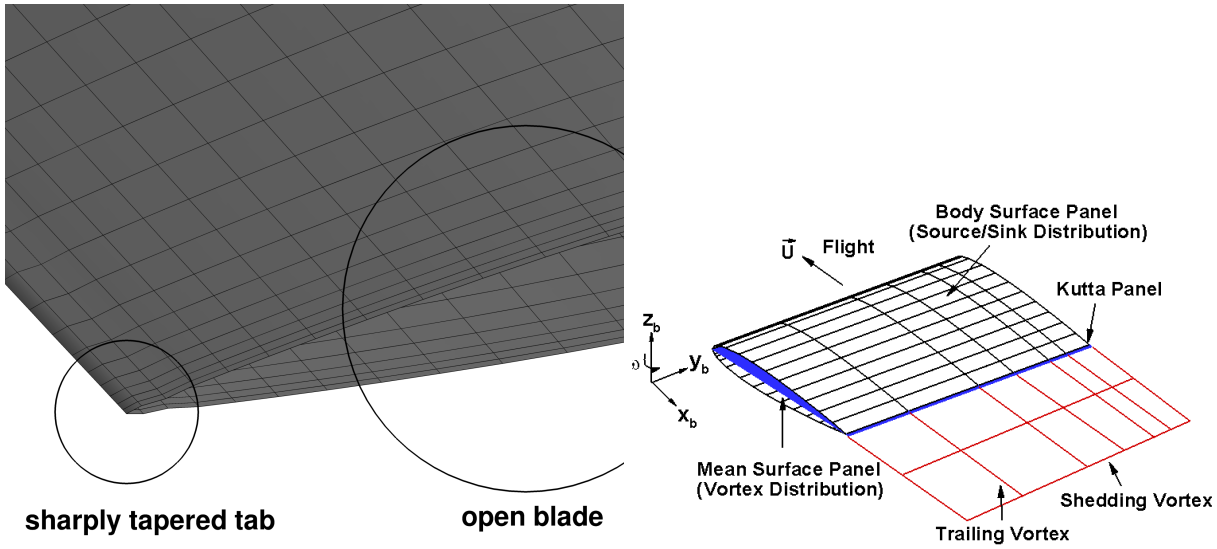

(a) [Blade tip of HARTII in UPM

(b) Schematic of UPM methodology

Figure 5. UPM discretization and methodology

With the set circulation, the strength on the Kutta panel is set and it is released at each time step into the wake. The wake then gradually evolves with time. The position of the released wake panels is then determined by the locally induced velocities on each wake panel, by all other panels in the flow. A roll-up model for the tip vortex is used to further accelerate the computation. To model viscous effects in the otherwise inviscid simulation, a vortex core radius is utilized, which is set to 0.3 of the chord length when released and which grows linearly with the time of the panel.

The fuselage in the UPM simulation is represented by a simple source/sink distribution to account for the displacement effect of the fuselage. For the HOST UPM coupling as well as UPM APSIM coupling, the data based output is scaled with the Prandtl-Glauert correction ($\sqrt{1-M^2}$), with the Mach number M being the local velocity at the respective panel.

III. RESULTS

The comparative papers from van der Wall et al.[7] and Smith et al.[2] both present the blade motion plots with a subtracted mean, which is also true for the airloads plots. The airloads are presented through the Mach number scaled normal force coefficient $c_n M^2$ at the location 87% blade radius. For consistency, this is also done in this paper. The results section is divided into three sections. First the grid sensitivity of the viscous CFD simulation is investigated, second the grid sensitivity of UPM simulation is analyzed and lastly both methods are directly compared against each other along with the inviscid CFD simulations. The flight condition of the HART II test case are listed in Table 6.

parameter	value
number of blades	4
rotor radius	$2m$
chord length	$0.121m$
flight speed	$33m/s$
rpm	1042
advance ratio	$\mu = 0.15$
temperature	$290.45K$
pressure	$100970Pa$
thrust	$3300N$
roll moment	$20Nm$
pitch moment	$-20Nm$
shaft angle	5.4^o
correction	-0.9^o

Table 6. Flight condition of the HART II rotor in descent flight.

A. CFD Grid Sensitivity Study

A grid sensitivity study is performed, where the effect of grid coarsening and refinement is analyzed with respect to the two CFD simulation strategies. All three levels of refinement are trimmed solutions with a restriction concerning the simulation on the finest grids. The trim solutions from the medium level are recycled to initialize the flow field and then one full coupling step is performed afterwards. This is acceptable as the changes are relatively small between the medium and fine mesh trim when looking at Table 7. Here the control angles of the various refinement levels and simulation techniques are listed along with the experimental values. For both simulations, JST and Hybrid, it is observed that the collective pitch angles θ_0 decreases with increasing grid density, while the cyclic pitch angles θ_c and θ_s vary without a clear pattern. These variations are about an order of magnitude smaller than the reduction of the collective pitch angle and therefore considered to be of minor influence.

pitch angle	$\theta_0[^o]$	$\theta_c[^o]$	$\theta_s[^o]$
experiment	3.80	1.92	-1.34
coarse (JST)	3.85	1.81	-1.02
medium (JST)	3.73	1.87	-0.96
fine (JST)	3.63	1.90	-1.03
coarse (Hybrid)	3.87	1.88	-1.07
medium (Hybrid)	3.72	1.86	-0.98
fine (Hybrid)	3.63	1.87	-0.99

Table 7. Trim angles at different grid densities and schemes

Moving onto the corresponding airload plots in Fig. 6 and Fig. 7 for the JST- and Hybrid simulations respectively, it is observed that the low-frequency content of the airloads is already well captured by the

coarse level simulations, also supported by the good correlation of the simulated mean airloads listed in Table 8. Yet, the prediction of required power is still significantly off for the coarse mesh setups. Potential reasons for the remaining discrepancies are the simplified structural modeling, the neglection of wind-tunnel interferences or the lack of laminar-turbulent transition in the simulation. The full high-frequency content only becomes available on the finest grid levels and the computed required power approaches the experimental value. The major difference between the JST and Hybrid scheme is that the amplitude of these frequencies are greatly enlarged for the Hybrid scheme. The amplitudes on the advancing side at $\psi \approx 45^o...90^o$ is even over predicted by the Hybrid scheme on the medium and fine mesh being clearly visible in the derivative plot. The amplitudes on the retreating side at $\psi \approx 285^o...315^o$ are not fully recovered by either JST or Hybrid scheme, but the Hybrid scheme comes closer to the experiment than the JST scheme.

	$c_n M^2$	req. power kW
experiment	0.0902	18.3
coarse (JST)	0.0762	31.4
medium (JST)	0.0795	22.0
fine (JST)	0.0779	21.3
coarse (Hybrid)	0.0762	31.5
medium (Hybrid)	0.0778	22.0
fine (Hybrid)	0.0789	21.4

Table 8. Mean airloads at different grid densities and schemes

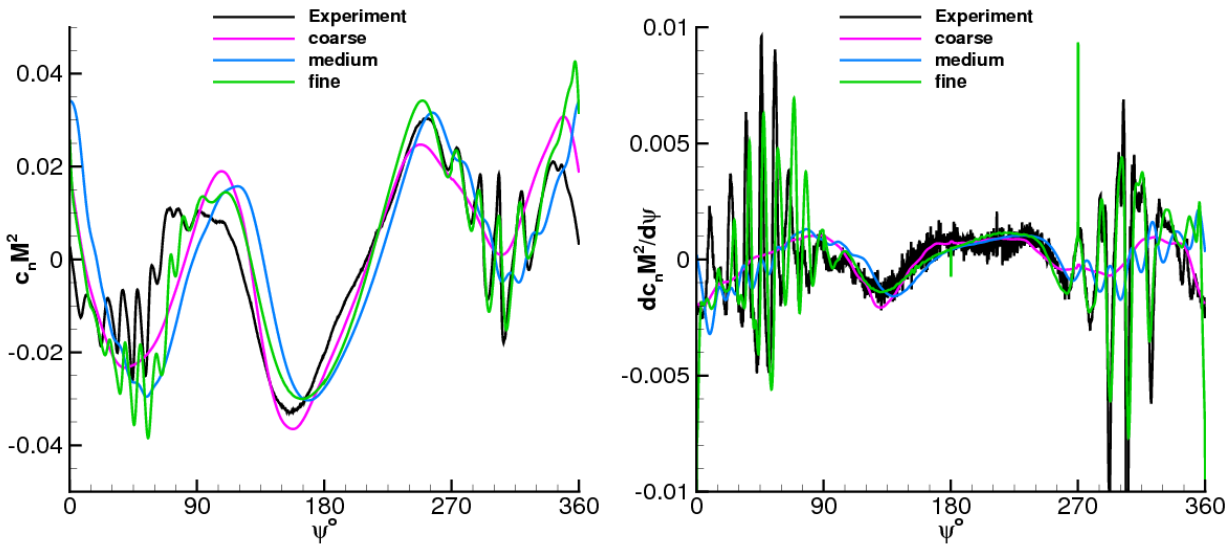

(a) airloads

(b) derivative of airloads

Figure 6. Comparison of airloads between experiment and different grid sizes for the JST simulation at $r/R = 87\%$.

The greater capturing of the amplitudes and the high-frequency content through the Pade scheme is grasped on a qualitative level, when looking at the vorticity plots of the two schemes on the finest mesh, Fig. 8. The Hybrid simulation not only resolves a lot more flow features, also the vortex strength is kept longer, while the vortex cores are sharper in contrast to the JST simulation. An example of this can be found in the downwash of the wake, where only the first trailing vortex shows the strong red for its vorticity, while this is still given two revolutions later for the Hybrid scheme.

As the goal of this simulation is to generate feasible data for the aero-acoustic simulation, the noise carpet plots of the experiment (Fig. 9) and the simulations (Fig. 10) are presented. On the coarsest grid level, the

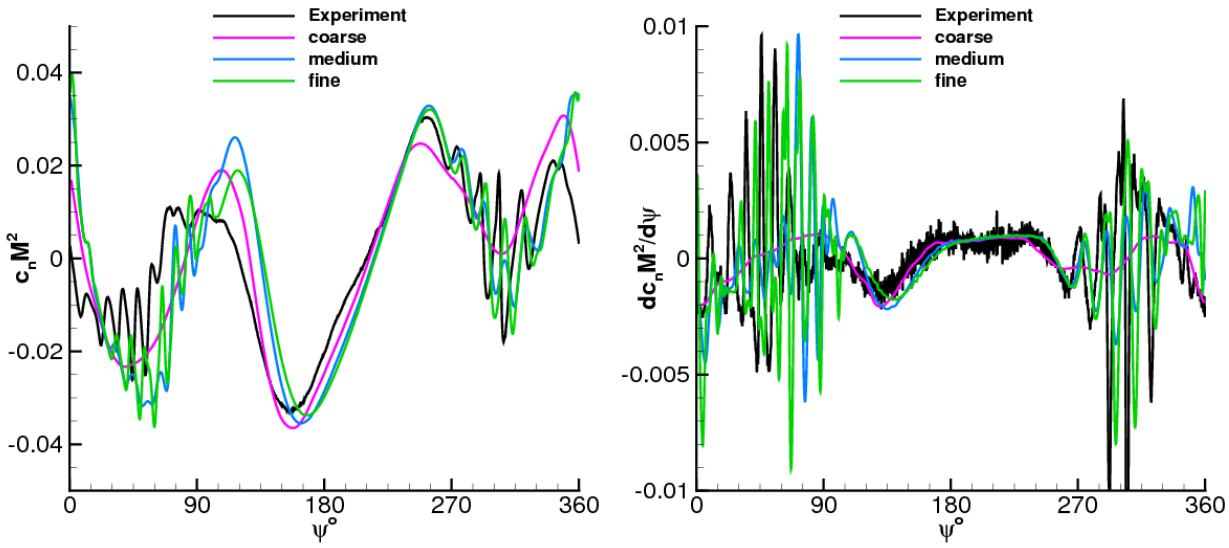

(a) airloads (b) derivative of airloads

Figure 7. Comparison of airloads between experiment and different grid sizes for the Hybrid simulation at $r/R = 87\%$.

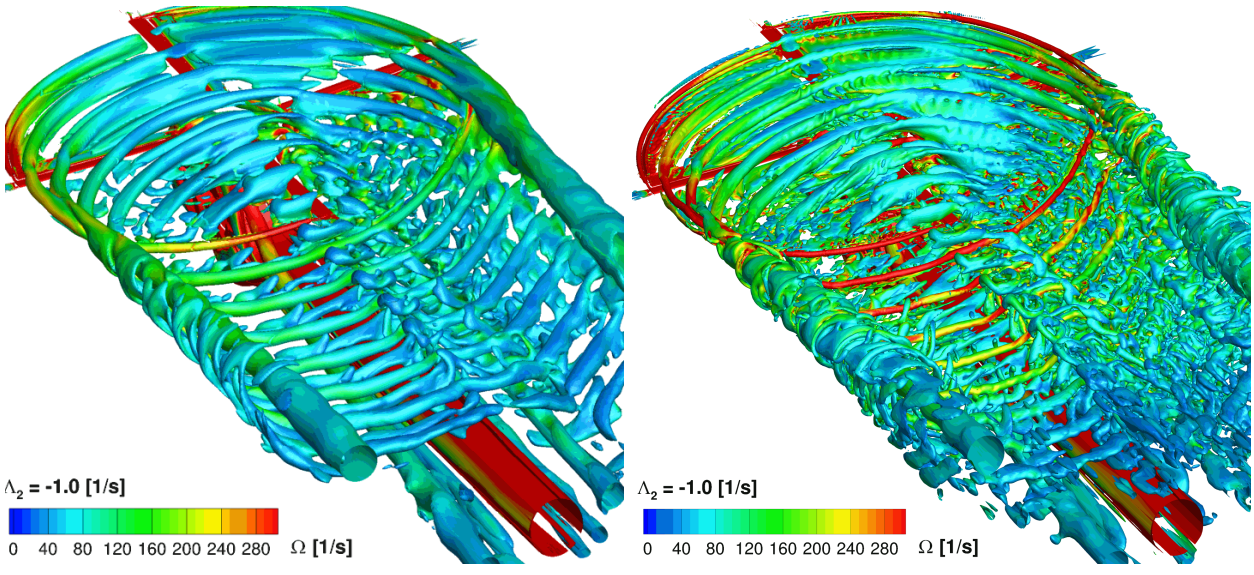

(a) JST (b) Hybrid

Figure 8. Vorticity plots of the fine mesh simulations.

noise levels are below the considered threshold of $85db$. Reason for this is that the vortex generation and conservation in the simulation is insufficient and only thickness and classical loading noise is observed. The high-frequency BVI noise cannot be represented as the load alternation from the vortices are already not captured in the airloads. On the medium mesh, the advantage of using the Hybrid scheme is seen and a difference of about $6dB$ is found between the peaks of the JST and Hybrid scheme. As for the directivity, it is also better captured by the Hybrid scheme resolving the two BVI hot spots. However, the hot spot on the retreating side is somewhat misrepresented as it splits into two single peaks in the elevated region. Looking at the finest grid simulations, the JST scheme also resolves the retreating side as a double peak at this level, which leads to the conclusion that this peak is likely occurring from the lack of the fuselage in the acoustic simulation as its shielding and scattering effects are neglected. The results on the finest mesh of the Hybrid scheme matches well with the experiment in contrast to the other simulations. The second hot spot on the retreating side is too small, but already achieves the peak value of $111db$.

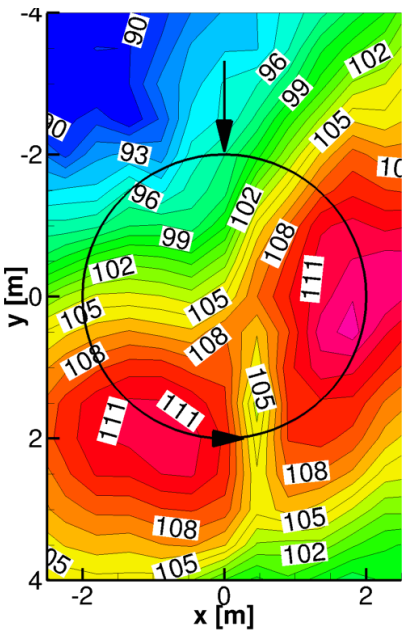

Figure 9. Noise carpet of the HART II baseline experiment. SPL at 6-40 BPF plotted.

As an estimator for the efficiency of the Hybrid scheme approach, the computational costs for one revolution are listed in Table 9. On the coarsest mesh, the Hybrid scheme even outperforms the JST scheme. Due to its tri-diagonal matrix, the solution is even quicker and the convergence rate is almost identical between the JST and Hybrid scheme. The advantage is lost on the finer grid levels as the blocking of the grid becomes make the implicit Pade scheme more and more inefficient. The stencil of the Pade scheme treats four cells at the boundary while in the field only two cells are treated; the filter even requires five cells at the boundary. In order to maintain the order, four dummy layers are required in contrast to two for the JST scheme, additionally increasing the resource demand and communication overhead. The finest mesh is highly blocked and therefore features a lot of block boundaries, thus more overhead is added slowing down the simulation. While the blocking is done manually and does not follow a strict rule, it is evident that with growing number of cells and grid blocks, the implicit Pade scheme becomes more expensive.

B. UPM Grid Sensitivity Study

The UPM grid sensitivity is investigated in a similar fashion as the CFD sensitivity study. In contrast to the CFD simulation, the trim solution is directly obtained from a HOST simulation using the prescribed wake model METAR. The utilized pitch control angles are thus presented in Table 10. The collective pitch angle θ_0 is well matched with the experiment, while the cyclic controls θ_c and θ_s are too little in their magnitude. However, the longitudinal control angle θ_s is slightly better than in the CFD computations.

Looking at the resulting airloads from these given blade motions in Fig. 11, it is seen that the integral

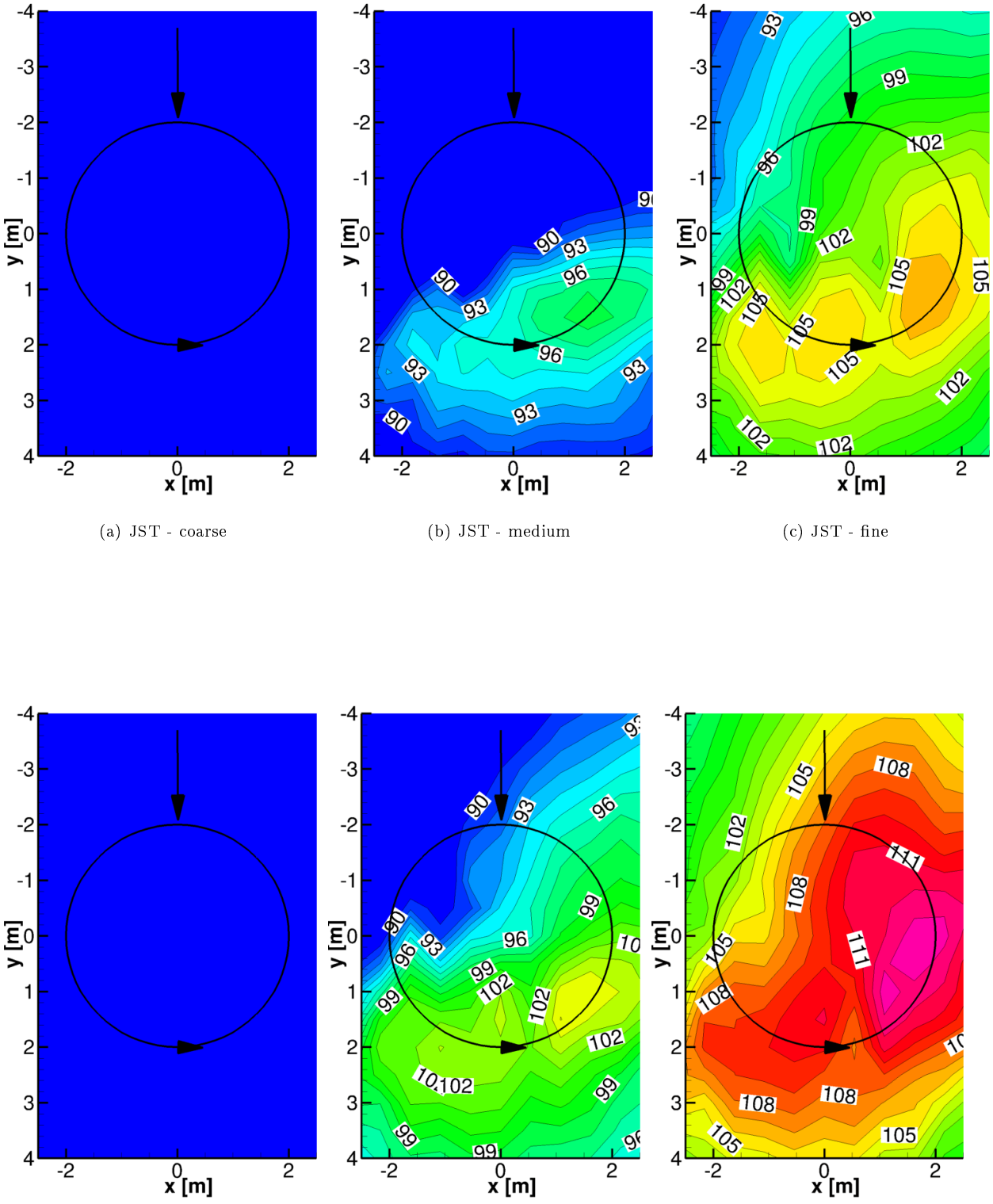

(a) JST - coarse

(b) JST - medium

(c) JST - fine

(d) Hybrid - coarse

(e) Hybrid - medium

(f) Hybrid - fine

Figure 10. Comparison of noise carpets for the different simulation strategies. SPL at 6-40 BPF plotted.

scheme/level	coarse	medium	fine
cores	24	72	384
blocks	84	174	500
JST (cpuh)	72	2,100	39,000
Hybrid (cpuh)	66	2,900	59,000
ratio	0.92	1.38	1.51

Table 9. Computational cost for one rotor revolution for different schemes and resolutions.

pitch angle	$\theta_0[^o]$	$\theta_c[^o]$	$\theta_s[^o]$
experiment	3.80	1.92	-1.34
coarse			
medium	3.78	1.71	-1.10
fine			

Table 10. Trim angles for the UPM simulations. NOTE: UPM is only coupled one way, the trim condition is obtained from a HOST using a prescribed wake model.

behavior is captured, yet the advancing side is noticeable underestimated. For the coarse mesh it is additionally observed that it deviates from the medium and fine mesh computations and resolves a too strong BVI peak on the advancing side. The mean $c_n M^2$ values are listed in Table 11. The agreement with the average value is better for UPM than the CFD simulations, but at the same time the required power is strongly underestimated. The reason for the higher mean $c_n M^2$ values is the neglected effect of re-trimming the rotor with UPM loads. When looking at the CFD simulations, the collective pitch angle lowers for increasing mesh resolutions. Since UPM is not re-trimmed, the mean thrust increases with increasing grid density. The underestimation of power arises from the lack of friction in UPM. The dissipative effect from under resolving the problem is also seen, since the coarse mesh computes the greatest required power value, while the finest mesh computes the smallest required power value.

	$c_n M^2$	req. power kW
experiment	0.0902	18.3
coarse	0.0952	11.23
medium	0.0939	9.50
fine	0.0978	9.35

Table 11. Mean airloads for UPM simulations

The evaluation of the noise carpets generated with UPM is plotted in Fig. 12. Already the coarse mesh shows the existence of both BVI hot spots. Increasing the resolution in UPM also increases the peak values of these hot spots. The medium mesh is just below the experimental peak values, while the fine mesh over predicts the peak value of the advancing side hot spot with about $1db$ and an overall larger area. Similar to the CFD simulations, the quiet zones of the sound carpet are not observed.

In Table 12 the required runtime for a single averaged UPM revolution is listed. The cost per rotor revolution may not be the most representable figure for UPM, since the wake evolves and grows with each revolution. Therefore the last revolution is also the most expensive revolution computed, because only then all wake panels are present. Since UPM is currently only executed on a single core, the runtimes are also identical with the CPU times. Similar to the CFD simulations, the cost for the coarsest mesh is diminishing in contrast to the finest mesh. Averaging the cost of the finest mesh over the revolutions, then 72 hours would be required to complete a single revolution. This cost is similar to the cost paid by the coarsest CFD simulations. Yet, the coarse CFD simulations do not predict any BVI, while the fine UPM simulations already overpredict it.

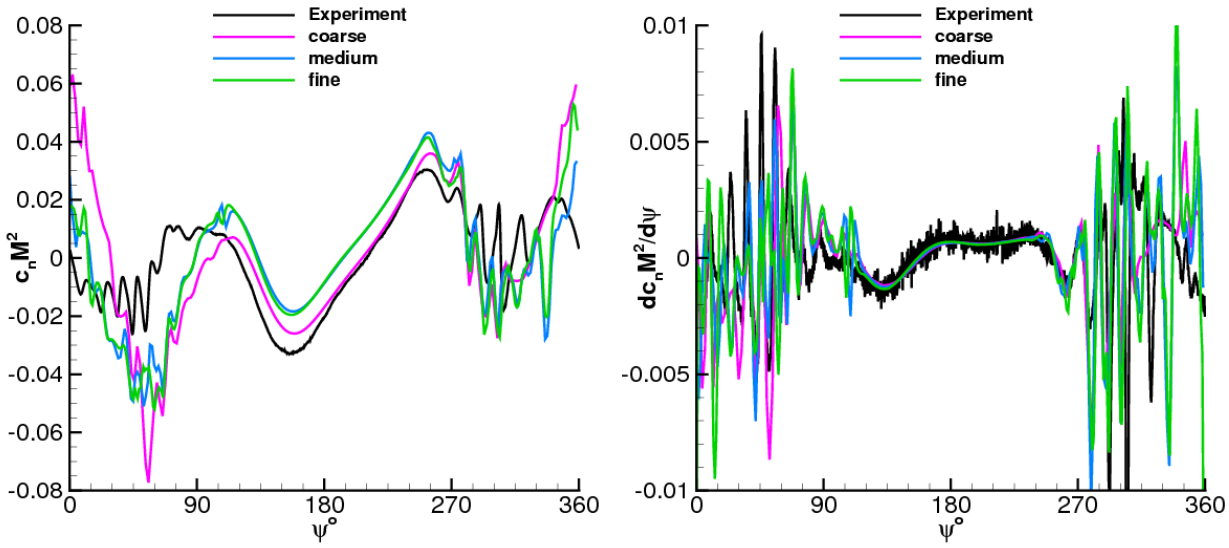

(a) airloads (b) derivative of airloads

Figure 11. Comparison of airloads between experiment and different grid sizes for the UPM simulation at $r/R = 87\%$.

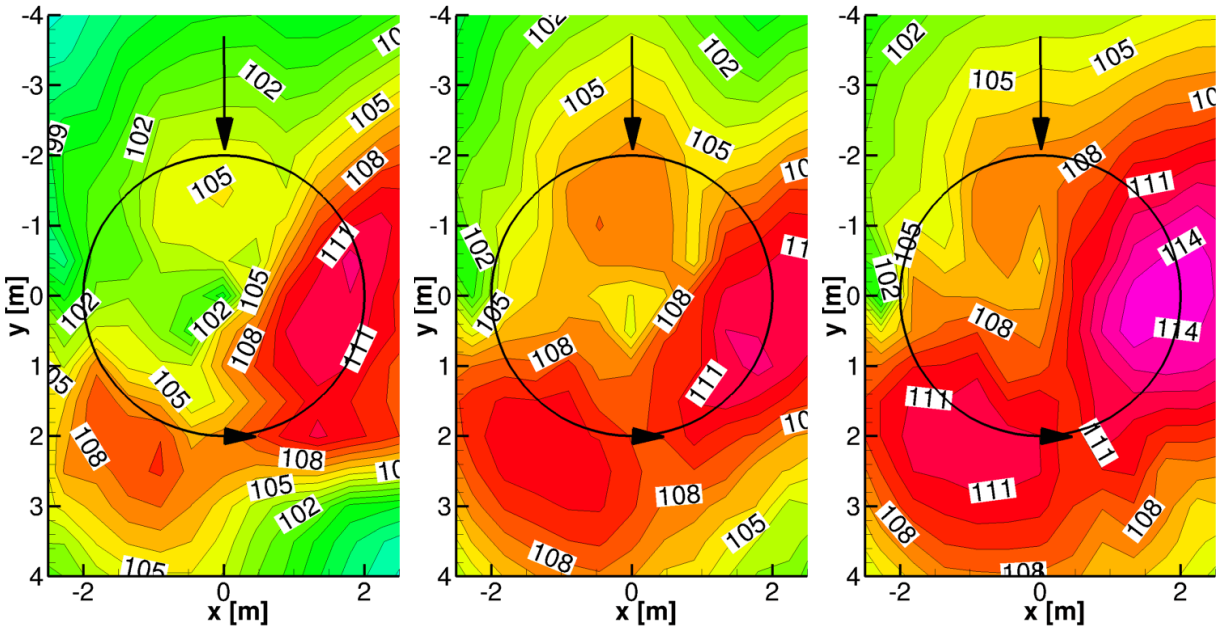

(a) UPM - coarse (b) UPM - medium (c) UPM - fine

Figure 12. Comparison of noise carpets for the different UPM simulations. SPL at 6-40 BPF plotted.

simulation	cpu time [h]	ratio
coarse	1.8	0.03
medium	12	0.17
fine	72	1.00

Table 12. Averaged computational cost for a single rotor revolution with UPM.

C. Method Comparison

In this section, the previously shown viscous CFD results on the medium mesh are compared against the results of the UPM simulation on the fine mesh and inviscid CFD simulations. The inviscid CFD simulations are also trimmed and are generated on the medium grid level. The trim control angles of the inviscid simulation are listed along with the UPM and viscous CFD results in Table 13. The collective pitch θ_0 angle is the lowest for the inviscid simulation, which is argued with the lack of phyiscal friction in the simulation. The rotor becomes more efficient and produces more thrust at a slightly lower angle. This effect has also been seen in the grid sensitivity study of the viscous meshes, where the effect of the numerical viscosity lowers for increasing grid density. The cyclic control angles θ_c and θ_s are closely aligned with the UPM results. The reason for this is that the fuselage has been neglected during the computation of trim control angles in both simulations, UPM and the inviscid CFD simulation.

pitch angle	$\theta_0[^o]$	$\theta_c[^o]$	$\theta_s[^o]$
experiment	3.80	1.92	-1.34
fine UPM	3.78	1.71	-1.10
inviscid CFD	3.60	1.68	-1.03
viscous CFD	3.72	1.86	-0.98

Table 13. Trim angles of different simulation strategies

The airloads plot is given in Fig. 13 with the subtracted mean listed in Table 14. The inviscid CFD simulation reports the lowest c_nM^2 mean value as well as required power. The mean value however, is in close vicinity of the viscous CFD simulation and thus attributed to minor inaccuracies during the trim procedure. Along with the resulting lower collective pitch θ_0, the required power becomes even smaller than the UPM result, which has not been re-trimmed and thus reports a noticeable larger c_nM^2 mean value. As for the azimuth distribution of c_nM^2, the absolute values are under predicted in the location of the BVI hot spots, with UPM having the largest offset, the inviscid CFD simulations in the middle, and the viscous CFD simulations with the least offset. For the derivative of the airloads, it is seen that the maximum peak value for the advancing side hot spot is over predicted by UPM. The inviscid CFD simulation shows the smallest peaks, while the viscous CFD simulation improves on the hot spot on the advancing side. However, all simulations show a phase shift to the experiment.

	c_nM^2	req. power kW
experiment	0.0902	18.3
fine UPM	0.0978	9.35
inviscid CFD	0.0765	4.83
viscous CFD	0.0778	22.0

Table 14. Mean airloads on medium mesh of different simulation strategies

Looking at the sound pressure level plots in Fig. 14, some correlation with the airloads derivatives is seen. For UPM, which features too large peak values in the derivative of the airloads, the peak value of the BVI hot spot on the advancing side is also over predicted. For the inviscid CFD simulation, the under prediction of the airloads peak is also resembled by the sound pressure level plot. The peak levels of the hot spots are too little, however the directivity is well matched with the experiment. In contrast the inviscid CFD simulation is quieter than the inviscid simulation, showing that the total, numerical and physical, viscosity disspate the vortices too quickly.

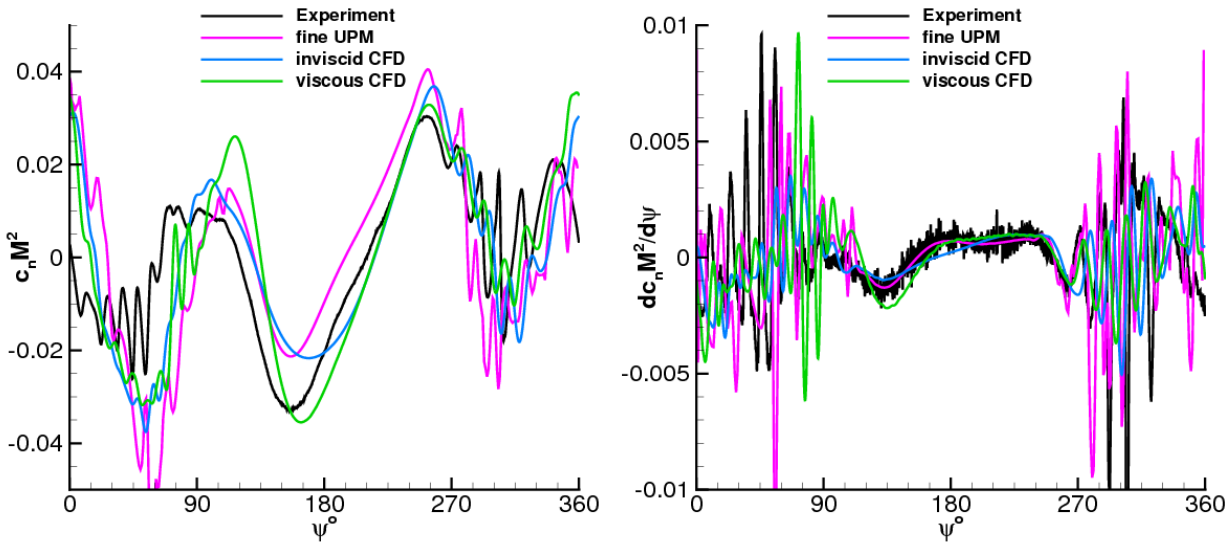

(a) airloads (b) derivative of airloads

Figure 13. Comparison of airloads between experiment and different simulation strategies at $r/R = 87\%$.

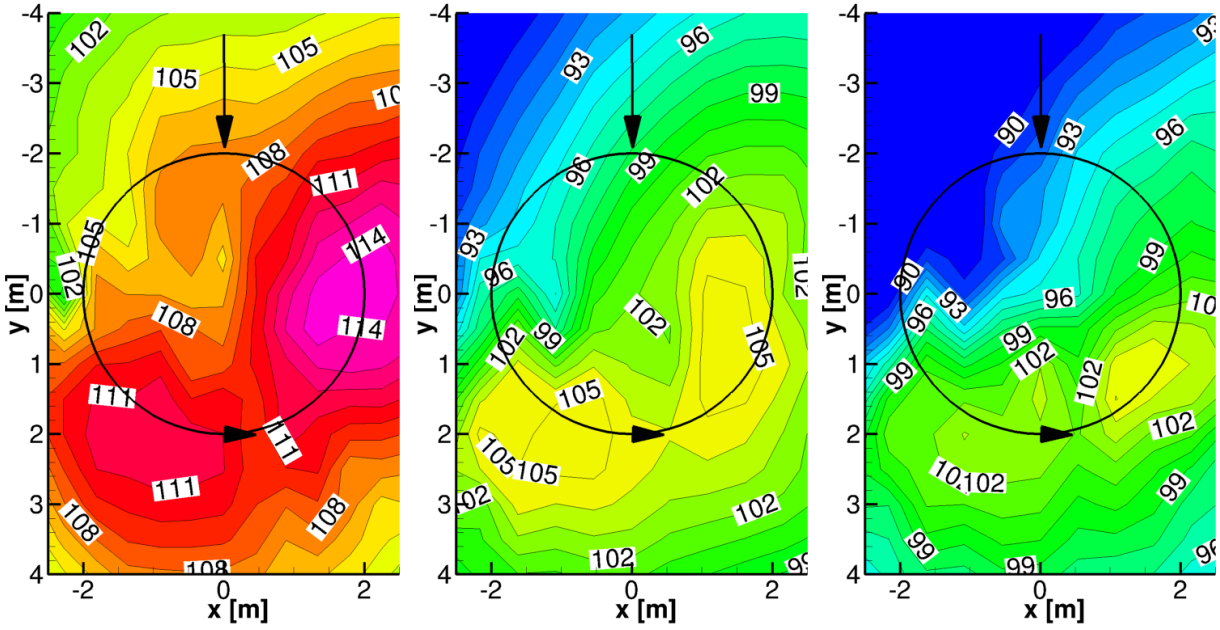

(a) UPM (b) inviscid CFD (c) viscous CFD

Figure 14. Comparison of noise carpets with different simulation techniques. SPL at 6-40 BPF plotted.

Similar to the previous investigations, the required resources for a rotor revolution are listed in Table 15 for the different simulations. The UPM cost per revolution may not be absolutely representable, since the last revolutions cost more than the first revolutions due to the evolving wake geometry. However, the cost is strongly reduced in contrast to the other CFD simulations. Thus, UPM features a good choice for wholesome parametric studies and may even be better than CFD for general validation. If budget is limited, then inviscid CFD simulations are recommended over viscous CFD simulation, since they show a better vortex preservation for the same grid size.

simulation	cpu time [h]	ratio
fine UPM	72	0.03
inviscid CFD	1,800	0.63
viscous CFD	2,900	1.00

Table 15. Computational cost for one rotor revolution for different simulation strategies.

IV. CONCLUSIONS

This paper reviews different techniques for the resolution of BVI noise. On the CFD side, the implicit compact Pade scheme of 4^{th} order has good vortex conservation properties and has therefore been tested for the simulation of the HART II baseline test case. It is applied to convect the vortices in the background mesh, while the rotor blades are still modelled with the JST scheme, referring to this method as Hybrid scheme. Opposing this technique, the unsteady panel method (UPM) with a free wake model is analyzed, which is computationally more efficient than the CFD simulations. Three studies are performed in this paper:

1. A benchmark of the Hybrid-Scheme with the traditional JST scheme is performed on three grid levels. It becomes clear that utilizing the Pade scheme in the background mesh allows for a much better resolution of the vorticity field surrounding the rotor. This again allows for a much better representation of the aero-acoustics. The cost increase is about 51% on the finest mesh setup, which when compared to other higher-order approaches is in a good standing.

2. A study using an inviscid, irrotational, incompressible panel code with a free wake model is undertaken for the HART II rotor. Already on the coarsest mesh setup, this code delivers reasonable results for the BVI noise. With increasing the grid density the noise levels also rise, an effect also observed for CFD. However, the computational effort also grows strongly. It ranges from about a working day to two weeks for the presented simulations

3. The previously investigated results are put into contrast with an inviscid CFD simulation featuring only 12 million grid points. From this analysis it is seen that when the computational budget is limited, the UPM code should be preferred and results should be validated with (fine) inviscid CFD simulations. However, a generalization of this fact may not be possible.

Future research should include:

- Further investigations of the aero-mechanical modelling to see whether the deviations in the noise carpets can be mitigated by employing a high-fidelity structural model. Also looking into modelling each blade individually due to the manufacturing differences may improve the results further.

- Broaden the research by applying the here presented methods to different rotor geometries such as the 7AD or ERATO blades, for which similar descent flight conditions have been examined.[25] With such a study, the feasibility of using UPM in rotor blade design applications could be clarified.

References

[1]B. G. van der Wall, "A Comprehensive Rotary-Wing Data Base for Code Validation: The HART II International Workshop," *The Aeronautical Journal*, Vol. 115, No. 1164, 2011, pp. 91–102.

[2]M. J. Smith, J. W. Lim, B. G. van der Wall, J. D. Baeder, R. T. Biedron, D. D. Boyd Jr, B. Jayaraman, S. N. Jung and B-Y Min, "An assessment of CFD/CSD prediction state-of-the-art using the HART II international workshop data," *68th Annual Forum of the American Helicopter Society*, 2012.

[3]J. W. Lim, A. Wissink, B. Jayaraman, and A. Dimanlig, "Helios Adaptive Mesh Refinement for HART II Rotor Wake Simulations," *Annual Forum 68 of the American Helicopters Society*, May 2012.

[4]R. K. Jain, J. W. Lim, and B. Jayaraman, "Modular Multisolver Approach for Efficient High-Fidelity Simulation of the HART II Rotor," *Journal of American Helicopter Society*, 2015.

[5]Y. Tanabe and H. Sugawara, "Construction and Validation of an Analysis Tool Chain for Rotorcraft Active Noise Reduction," *38th European Rotorcraft Forum*, 2012.

[6]U. Kowarsch, "Aeroacoustic Simulation of a Complete H145 Helicopter in Descent Flight," *41st European Rotorcraft Forum*, 2015.

[7]B. G. van der Wall, S. N. Jung, J. W. Lim, M. J. Smith, J. Bailly, J. D. Baeder, and D. D. Boyd, Jr., "An Assessment of Comprehensive Code Prediction State-of-the-Art Using the HART II International Workshop Data," *Annual Forum 68 of the American Helicopters Society*, 2012.

[8]J. Yin, B. v. d. W. and Wilke, G., "Rotor noise radiation under influence of blade deformation, compressibility and different fuselage modelling," *Journal of Sound and Vibration*, Vol. 357, 2015, pp. 115–116.

[9]Sanjiva K. Lele, "Compact finite difference schemes with spectral-like resolution," *Journal of Computational Physics*, Vol. 103, No. 1, 1992, pp. 16 – 42.

[10]A. Jameson, W. Schmidt, and E. Turkel, "Numerical Solution of the Euler Equations by Finite Volume Methods Using Runge-Kutta Time-Stepping Schemes," *14th AIAA Fluid and Plasma Dynamics Conference*, 1981.

[11]B. Benoit, A.-M. Dequin, K. Kampa, W. von Grünhagen, P.-M. Basset, and B. Gimonet, "HOST, a General Helicopter Simulation Tool for Germany and France," *56th Annual Forum of the American Helicopters Society*, 2000.

[12]J. Raddatz, and J. Fassbender, "Block structured Navier-Stokes solver FLOWer. MEGAFLOW - Numerical Flow Simulation for Aircraft Design," *Notes on Numerical Fluid Mechanics and Multidisciplinary Design*, Vol. 89, 2005, pp. 27–44.

[13]S. R. Ahmed, and V. T. Vidjaja, "Unsteady Panel Method Calculation of Pressure Distribution on BO 105 Model Rotor Blades," *50th Annual Forum of the American Helicopters Society*, 1994.

[14]M. Dietz, W. Khier, B. Knutzen, S. Wagner, and E. Krämer, "Numerical Simulation of a Full Helicopter Configuration Using Weak Fluid-Structure Coupling," *American Institute of Aeronautics and Astronautics*, 2007.

[15]C. C. Hennes and K. S. Brentner, "The Effect of Blade Deformation on Rotorcraft Acoustics," *31st European Rotorcraft Forum*, 2005.

[16]J. Yin, and J. Delfs, "Improvement of DLR Rotor Aeroacoustic Code (APSIM) and its Validation with Analytic Solution," *29th European Rotorcraft Forum*, 2003.

[17]D. C. Wilcox, *Turbulence Modeling for CFD, 2nd ed.*, DCW Industries, Inc, 1998.

[18]C. B. Allen, "CHIMERA volume grid generation within the EROS code," *Proceedings of the Institution of Mechanical Engineers, Part G: Journal of Aerospace Engineering*, Vol. 214, 2000, pp. 125–140.

[19]M. R. Visbal and D. V. Gaitonde, "On the Use of Higher-Order Finite-Difference Schemes on Curvilinear and Deforming Meshes," *Journal of Computational Physics*, Vol. 181, No. 1, 2002, pp. 155 – 185.

[20]S. Enk, *Zellzentriertes Padeverfahren für DNS und LES*, Ph.D. thesis, Technische Universität Carolo-Wilhelmina Braunschweig, 2015.

[21]S. E. Sherer and J. N. Scott, "High-order compact finite-difference methods on general overset grids," *Journal of Computational Physics*, Vol. 210, No. 2, 2005, pp. 459 – 496.

[22]K. Pahlke, and B. van der Wall, "Progress in weak fluid-structure-coupling for multi-bladed rotors in high-speed forward flight," *28th European Rotorcraft Forum*, 2002.

[23]G. Arnaud, and P. Beaumier, "Validation of R85/Metar on the Puma RAE Flight Tests," *18th European Rotorcraft Forum*, 1992.

[24]of Naval Research, O., of Michigan, U., and Council, N. R., *Eighteenth Symposium on Naval Hydrodynamics*, National Academies Press, 1991.

[25]B.G. van der Wall, C. Kessler, Y. Delrieux, P. Beaumier, M. Gervais, J-F Hirsch, K. Pengel, and P. Crozier, "From ERATO Basic Research to the Blue Edge Rotor Blade," *AHS International 72nd Annual Forum & Technology Display*, 2016.